Manuscript ID: DOEBTO-UMD-9158-26-MM1

Full Citation: M. V. P. Menezes, A.-H. Othman, J. Tancabel, and V. C. Aute, "**An approach for fast and accurate simulation of phase change material based thermal energy storage in buildings**," *Journal of Energy Storage*, vol. 152, p. 120384, Mar. 2026, DOI: 10.1016/j.est.2026.120384.

An Approach for Fast and Accurate Simulation of Phase Change Material based Thermal Energy Storage in Buildings

Mylena V.P. Menezes, Al-Hussain Othman, James Tancabel, Vikrant C. Aute*

Department of Mechanical Engineering, University of Maryland, College Park, USA

*Corresponding author: vikrant@umd.edu

Abstract: Latent heat thermal energy storage (LHTES) has significant potential for mitigating peak electricity demand and enabling load shifting in buildings. Phase Change Material embedded heat exchangers (PCM-HX) can significantly improve energy demand management due to high storage capacity. However, PCM-HX evaluation typically depends on computationally expensive fully transient simulations, posing significant challenges for scalable system- and building-level energy assessments across different climates and system architectures. This paper presents a generalized, accurate, and computationally efficient methodology for simulating building energy systems integrated with LHTES. The PCM-HX transient performance is represented by performance maps generated using a Generalized Resistance-Capacitance Model (GRCM) that enables accurate predictions of arbitrary PCM-HXs at low computational cost. The feasibility of the proposed approach was verified using a case study considering a dual-mode heat pump-thermal energy storage (HP-TES) system simulated in Modelica with Spawn of EnergyPlus™ for a DOE prototype small-office building in two locations: Tampa, FL, and International Falls, MN. The PCM-HX performance maps provided accurate predictions of PCM-HX transient behavior, with mean absolute percentage deviations within 2-4% compared to GRCM while also achieving at least 1800x reduction in computational time. Moreover, the HP-TES system achieved energy savings of up to 17.4% in Tampa, FL, and 62.2% in International Falls, MN, demonstrating the broader applicability of the proposed methodology across different climate zones. This work highlights the importance of robust PCM-HX models in enabling accurate and computationally

efficient building-level simulations and enabling future research opportunities for investigating optimized HP-TES designs and advanced control strategies for grid-interactive buildings.

Keywords: Thermal Energy Storage; Phase Change Material; Resistance-Capacitance Model; Performance Maps; Modelica; Building Simulation

Highlights:

- New approach enables rapid and accurate building energy simulation with PCM
- PCM performance maps generated using a novel, generalized thermal network model
- Performance maps in Modelica are at least 1800x faster than full PCM-HX simulations
- Methodology is broadly applicable to any climate and system configuration
- Enables fast TES system design, evaluation and controls development

B	Matrix of boundary heat flow (W)	PCM	Phase Change Material
C	Thermal Capacitance (J/K)	RCM	Resistance-Capacitance Model
c_p	Specific Heat (J/kg-K)	RMSE	Root Mean Square Error
CV(RMSE)	Coefficient of Variation of Root Mean Square Error	ROM	Reduced-Order Model
H	Latent Heat (kJ/kg)	SOC	State of Charge
k	Thermal Conductivity (W/m-K)	TES	Thermal Energy Storage
L	Distance between staggered tubes (m)	TOU	Time of use
LMTD	Log mean temperature difference (K)	**Greek Symbols**	
$\dot{m}$	Mass Flow Rate (kg/s)	γ	Porosity (-)
M	Matrix of internal heat flow (W)	δ	Thickness (m)
T	Temperature (K)	Δ	Variation (-)
t	Time (s, h)	ρ	Density (kg/m^3)
$\dot{T}$	Time Derivative of Temperature (K/s)	**Subscripts**	
V	Volume (m^3)	CF	Curve-fit
x	Liquid Fraction (-)	eff	effective
Abbreviations		f	final
BPHX	Brazed plate heat exchanger	i	Initial/index
GRCM	Generalized Resistance-Capacitance Model	long	longitudinal

HP	Heat Pump	melt	melting
HX	Heat Exchanger	sol	solidification
LHTES	Latent Heat Thermal Energy Storage	Stor	Stored
MCHX	Microchannel heat exchanger	vert	vertical

1. Introduction

The growing demand for more efficient renewable and sustainable technologies to mitigate the implications of climate change has attracted significant research interest. While renewable energy sources such as solar and wind have seen notable growth in the electricity sector, their inherent intermittency continues to pose a significant challenge to widespread implementation [1]. The U.S. Energy Information Administration reports that the residential and commercial sectors account for nearly 40% of total energy consumption and 35% of carbon emissions [2]. Traditional heating and cooling systems, primarily powered by fossil fuel-based electricity, contribute substantially to these emissions. In 2022, carbon emissions from building operations reached nearly 10 gigatons, marking the largest annual increase observed over the past decade [3]. Heat pumps (HPs) have emerged as one of the key solutions for reducing energy use and mitigating carbon emissions in space conditioning. Global adoption of HPs, air conditioners and refrigeration systems is expected to increase over 6 billion units by 2050 [4]. However, the electricity demand for residential and commercial cooling and heating can rise substantially with the use of HP systems, particularly in extreme weather locations [5]. To mitigate this increased demand, strategies focused on renewable energy generation, demand curtailment and load shifting can help reduce grid stress without significant additional costs.

Coupling heat pumps with thermal energy storage (HP-TES) offers a promising solution for load shifting, helping to reduce the mismatch between energy supply and demand [6]. TES systems can recharge during low-demand periods and supply stored energy during peak demand, thereby smoothing grid fluctuations [7], [8]. By shifting peak building loads to off-peak periods, HP-TES can also lower electricity costs and enhance the utilization of power generation infrastructure [9]. Latent heat thermal energy storage (LHTES) using phase change materials (PCMs) is particularly effective for storing surplus energy and mitigating energy fluctuations [10], [11]. HP-TES systems incorporating PCMs are gaining attention due to their high latent heat of fusion, which enables efficient thermal energy storage for power supply [12]. Huang et al. [13] proposed a cascade heat pump system integrated with TES using PCMs as intermediate HX between indoor and outdoor coils. A steady-state surrogate model was utilized to predict the heat transfer rates during the charging and discharging of a salt hydrate PCM, which provided more peak electricity load reduction at lower charging costs compared to ice. Du et al. [14] proposed an air-source HP-TES system for space heating where PCM discharges heat to circulating water, which demonstrated higher storage capacity and heating power compared to ice/chilled water TES systems. An integrated air source HP-TES simulated by Sun et al. [15] was shown to effectively shift power consumption during a 3.5-hour peak load period.

However, the transient nature of PCM heat transfer often requires computationally expensive methods to accurately predict the charging and discharging process in PCM embedded heat exchangers (PCM-HX), and can be one of the drawbacks of system-level simulation and large-scale optimization strategies. Most numerical models of PCM-HX rely on Computational Fluid Dynamics (CFD) to capture complex, time-dependent physical phenomena such as 3D heat conduction, natural and forced convection [16]. While CFD provides high-fidelity results by solving the energy and mass conservation equations, this requires iterative calculations, which are highly computationally intensive. To this end, reduced-order models (ROMs) can be used to reliably predict PCM-HX performance in a computationally-efficient manner, allowing for testing multiple heat exchanger configurations with minimal accuracy penalty [17]. For instance, Bacellar et al. [18] proposed a ROM where CFD results were utilized to develop curve fits that correlated PCM temperature and liquid fraction. The authors reported that the ROM showed excellent agreement with CFD simulations with a 250,000x speed-up.

Resistance-Capacitance Models (RCMs), have increased popularity for evaluating the performance of PCM-HXs due to their balance between accuracy and computational efficiency. Unlike CFD models, which solve time-dependent partial differential equations to capture detailed heat transfer and fluid flow phenomena, RCMs simplify the PCM-HX into a network of thermal resistances and capacitances, analogous to an electrical circuit [19]. As a result, RCMs are particularly well-suited for parametric studies and integration with building energy simulation tools, in which fast and reasonably accurate performance estimation is required [20]. Gao et al. [21] used a RC network to analyze shape-stabilized phase change materials, reporting that the average errors in surface temperature and heat flux predictions are 0.42°C and 15%, respectively, when compared to experimental data. Neumann et al. [22] developed an RCM for a PCM-embedded plate heat exchanger where the outlet fluid and PCM temperature deviations compared to a finite-element model were 0.62 K and 0.85 K, respectively, with the benefit of a 20-30x reduction in computational time. An RCM for melting in periodic structure was developed and validated against experimental data by Alam et al. [23], showing a mean temperature deviation range between 1.34 K to 2.81 K. The authors highlighted that the speed-up factor was 10^4x faster than CFD simulations. Wan et al. [24] investigated quasi-2D RCM for partially charging/discharging PCM storage tank. Compared to effectiveness-NTU, the computation time was about 10% lower in this new proposed model. Yin et al. [25] proposed a RCM model for analyze the melting stage of a single finned tube for high-energy airborne weapons. Compared with the experiment, the maximum temperature error of outlet temperature is 4.9%, and the average temperature error is 1.2%. Menezes et al. [26] verified and validated a generalized RCM for the prediction of an arbitrary RC network for three different PCM-HXs configurations. The model presented excellent agreement compared to CFD model, with mean PCM temperature deviation between 0.56 – 0.73 K for a single-slabbed microchannel PCM-HX melting case.

Despite the growing success of RCMs and other ROMs in standalone thermal performance evaluations of PCM-HX, their integration into building-level simulation platforms remains limited, as few studies have leveraged ROMs for predicting TES performance in the context of dynamic building environments while maintaining low computational cost. Wang et al. [27] proposed a novel RCM for building envelope calculation, which has shown an efficiency improvement of approximately 78% compared to EnergyPlus™. Kamal et al. [28] proposed a control strategy and cost optimization approach for an HP-TES system using the EnergyPlus™ built-in TES model with ice as the storage medium to avoid the complexity of detailed PCM-HX simulations. However, EnergyPlus™ currently supports only ice storage systems in active cooling/heating applications, limiting its applicability to broader PCM-based systems [28]. The development of performance maps in the form of polynomial expressions to characterize HP or TES equipment provides flexibility and simplicity since it increases the number of possible scenarios in which these component maps can be useful [29]. RCM map-based models enable rapid prediction of discharge and recharge behavior, supporting broader application of PCM-HX for TES in transient simulations; however, such models cannot be directly implemented in EnergyPlus™ due to the optimal control methodology employed in this software [30]. Therefore, further studies are needed to dynamically simulate HP systems integrated with PCM-TES, enhancing their practicality for real-time control and optimization scenarios while reducing computational cost. In this context, Homod et al. [31], [32] applied reinforcement learning to optimize the utilization of TES system in reducing grid stress, demonstrating energy savings of more than 28% compared to traditional PID control. However, this approach has limited generalizability for designing TES integrated into building energy systems across different climatic conditions, PCM types, and system architectures, as its robustness is restricted to specific field-test operating data, locations, and building types.

In this paper, we propose a methodology for accurate and computationally efficient simulation of building energy systems integrated with LHTES for broader applicability in different system architectures. The approach utilizes polynomial-based performance maps generated from a Generalized Resistance-Capacitance Model (GRCM) to predict the transient behavior of any type of PCM material [26]. The resulting models enable rapid evaluation of the suitability and operational flexibility of PCM for HP-TES applications in both cooling and heating modes. A case study was conducted to demonstrate the feasibility of the proposed methodology in effectively simulate a HP-TES for space conditioning. A 5-ton (~17.5 kW) air-to-water HP integrated with PCM-based LHTES is designed to meet both cooling and heating demands of a DOE prototype of a small commercial building and is implemented as a custom component in EnergyPlus™ through Spawn. Simulations were carried out across two representative ASHRAE climate zones using typical meteorological year (TMY3) [33] data to demonstrate the broader applicability of the methodology across multiple climate zones: Tampa, Florida (2A), for cooling conditions and International Falls, Minnesota (7), under heating conditions.

The remainder of this paper is organized as follows: Section 2 presents the methodology for PCM-HX design, the description of the proposed PCM-HX and HP performance maps, and introduces the case study used to verify the proposed methodology. Section 3 presents the PCM-HX component simulation, performance map generation, and verification with Modelica component models, and case study results. The conclusions are presented in Section 4.

2. Methodology

Figure 1 shows the schematic of the HP-TES integration coupling PCM performance maps, Modelica and EnergyPlus™. The PCM-HX integration with HP leverages the predictive capabilities of the GRCM [26] to simulate PCM-HX thermal performance, enabling its implementation in Modelica. Based on design-day building loads, the PCM-HX was dimensioned for the target HP-TES application using GRCM. The resulting GRCM outputs were used as source data to construct TES performance maps, which were subsequently embedded in the Modelica simulations to represent the PCM-HX component within the HP-TES. The Modelica Buildings Library [34], [35] was used to construct the building model (e.g., thermal zones) and supervisory control logic (e.g., switches, Boolean operations, logic gates). In parallel, building loads were computed using Spawn of EnergyPlus™ [34], while Dymola [36] provided the dynamic simulation environment coupling EnergyPlus™, the PCM performance maps, HVAC operation and rule-based control. Moreover, system-level performance maps were developed based on transient component and system models to enable faster analysis simulations. The HP-TES operation and rule-based control follows the time of use (TOU) hours of the target locations and the PCM state of charge (SOC). The control objective was a demand reduction strategy, in which the TES reduces building load during peak demand periods and/or when the PCM is fully depleted. During off-peak hours, the TES is recharged to enable effective load shifting for subsequent operation. This integrated framework enables a comprehensive evaluation of HP-TES performance in meeting building thermal demands under varying climatic conditions, applicable to any kind of system architecture.

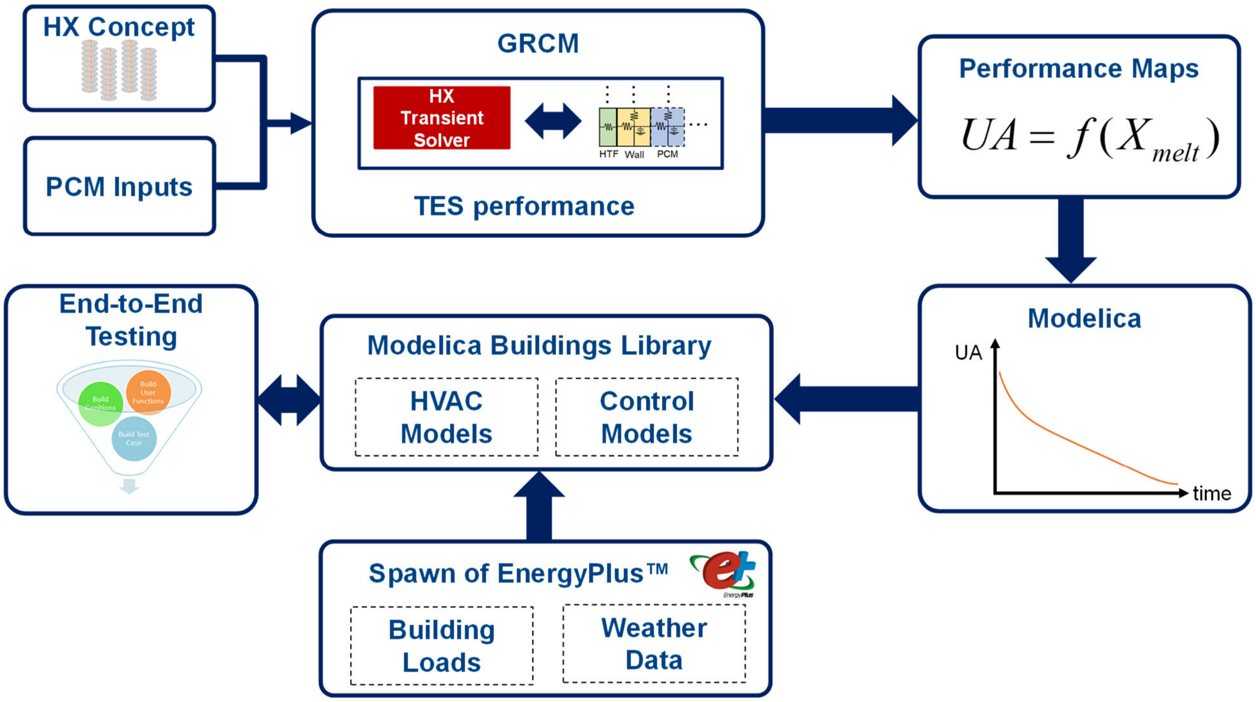

Figure 1. Workflow of the proposed methodology coupling PCM performance maps, Modelica and EnergyPlus™

2.1 PCM-HX Design

The PCM-HXs represent the TES component in the HP-TES integration and must be sized to meet the required storage capacity (i.e., operating time) and discharge/recharge rate in both cooling and heating modes (i.e., building load). The PCM-HXs were sized to meet the space conditioning loads for three hours in two US climate zones: Tampa, FL (2A) and International Falls, MN (7), under cooling and heating conditions, respectively. Table 1 presents the heating and cooling loads for a DOE small office prototypical building [37], determined based on design day conditions for the target locations specified in this study according to ASHRAE Standard 90.1-2022 [38].

Table 1. Heating and cooling loads based on ASHRAE Standard 90.1-2022 [38].

City (ASHRAE Climate Zone)	Heating Design Load (kW)	Cooling Design Load (kW)
Tampa, FL (2A)	5.9	16.3
International Falls, MN (7)	16.5	14.3

The PCM storage capacity was determined using Eq.(1), in which the maximum required discharge rate is for the cooling mode, accounting for the maximum cooling capacity based on AHRI 2010/240 A-test operating conditions.

$$V_{PCM} = \frac{\int_{t_i}^{t_f} \dot{Q} dt}{\rho_{PCM} H_{Latent}} \tag{1}$$

A staggered round-tube plate-fin heat exchanger was selected due to its high heat transfer performance, compactness, and commercial availability, ensuring suitability for air conditioning and TES applications where space and thermal efficiency are critical [39]. The PCM-HX configuration is shown in Figure 2, where the container is assumed to be well insulated, and the container wall is considered adiabatic.

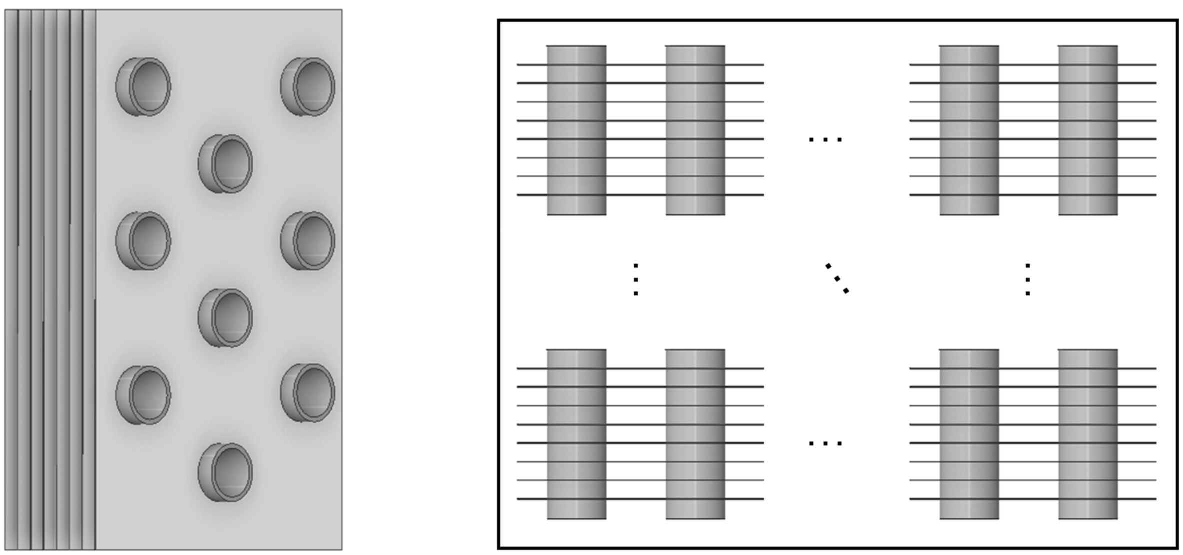

Figure 2. (Left) Sample round-tube plate-fin HX; (Right) Thermal battery array schematic

The required PCM-TES surface area was determined using the UA-LMTD approach to satisfy the maximum capacity required by the HP-TES system (~17.5 kW). The fin density (FPI) was selected to ensure sufficient surface area to meet the *UA* requirement while maintaining adequate PCM volume. These calculations provided the internal HX volume and PCM availability (porosity), which were then used to establish the number of PCM-HXs required to deliver the TES storage capacity and discharge/recharge time. Pressure drop across the fluid flow tubes, evaluated using Churchill correlation [40], and pumping power requirements were also included. The capacity of the PCM-HX was adjusted to meet the target thermal load by scaling the number of PCM-HX units while preserving the same geometric design. The design parameters of the thermal battery are provided in Table 2.

Table 2. Structural size of the thermal battery for heating and cooling modes

Measure	Unit	Heating PCM-HX	Cooling PCM-HX
Horizontal Spacing (HS)	mm	31.3	30.3
Vertical Spacing (VS)	mm	28.8	26.5
Tube Length	m	0.95	0.92
Outer Tube Diameter (OD)	mm	9.3	9.3
Inner Tube Diameter (ID)	mm	8.9	8.9
Tube thickness	mm	0.33	0.33
FPI	-	13	14
Fin thickness	mm	0.10	0.10
Porosity	%	87.4	86.2
Distance between tubes (L)	m	0.015	0.013

The equivalent distance between HX tubes for all calculations is defined as shown in Eq.(2):

$$L_h = \frac{\sqrt{(VS-OD)^2+(HS-OD)^2}}{2} \tag{2}$$

Organic PCMs A36 and A12 [41] were used for heating and cooling modes, respectively, and their thermophysical properties are shown in Table 3. For each PCM, a temperature glide of ±2 K is assumed, where fully charged (SOC = 1, fully liquid PCM) occurs at $T = T_{nominal} + 2$ and fully discharged state (SOC = 0, fully solid PCM) occurs at $T = T_{nominal} - 2$.

Table 3. PCM thermophysical properties

Property	Unit	A36 [41]	A12 [41]
k (Solid & Liquid)	W/mK	0.22	0.22
c_p (Solid & Liquid)	kJ/kgK	2.3	2.16

Latent Heat	kJ/kg	250	215
ρ (Solid & Liquid)	kg/m³	776	775
Melting Temperature Range	°C	34-38	10-14

2.2 Generalized Resistance-Capacitance Model

An experimentally-validated Generalized Resistance-Capacitance Model (GRCM) that enables high-fidelity, low computational cost predictions of the arbitrary PCM-HX performance was utilized to generate the source data used to construct the performance maps considered herein [26]. The GRCM was verified and validated using three different cases: a single-slabbed finned PCM-HX, a copper foam/paraffin HX and a straight tube annular finned HX. The validations showed that the predicted outlet water temperature matched really well with experimental data for the annular finned HX, with mean HTF temperature deviation of 0.24 K and 0.34 K for melting and solidification processes, respectively. The differences between simulation and experimental results are likely attributable to heat losses to the environment caused by imperfect insulation of the PCM-HX.

The GRCM assumptions include:

- In the PCM, conduction is the dominant heat transfer mode and natural convection effects are neglected;
- No mass transfer across segments;
- Contact resistance between PCM and metal was neglected;
- Constant PCM thermophysical properties throughout the domain;
- Adiabatic TES container walls.

Figure 3 shows a fin-tube PCM-HX which is representative of the TES design presented herein, along with the two-dimensional thermal resistance-capacitance network with conjugate heat transfer boundary conditions simulated with the GRCM.

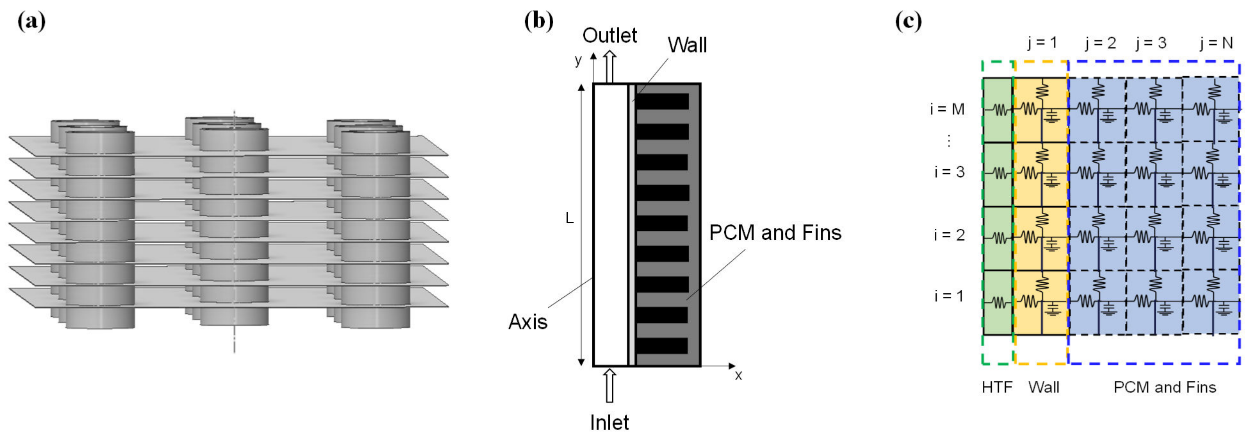

Figure 3. Schematic of PCM-HX for a conjugate heat transfer in GRCM (a) Plate-Fin HX; (b) Axisymmetric domain for each tube; (c) RC-Network

2.3 System Performance Modeling

2.3.1 Thermal Energy Storage Level Performance Maps

The charging and discharging performance of a PCM storage unit is traditionally modeled in EnergyPlus™ using polynomial expressions that establish the relationships between different parameters in the unit [30]. King and Potter [42] first developed the polynomial fits required to calculate ice-on-coil melting in EnergyPlus™ based on liquid fraction and log mean temperature difference (LMTD) between the brine and the storage freezing temperature, as shown in Eq. (3).

$$UA_{ice} = (C_1 + C_2 \cdot x_{melt} + C_3 \cdot x_{melt}{}^2 + C_4 \cdot x_{melt}{}^3 + C_5 \cdot x_{melt}{}^4 + C_6 \cdot x_{melt}{}^5) \cdot Q_{stor} / \Delta t / LMTD \qquad (3)$$

in which the C_i are the fitted polynomial coefficients based on the manufacturer data of an ice-on-coil HX, Q_{stor} is the nominal storage capacity, and Δt is the simulation time interval. Their resulting performance curves were validated against ice thermal storage [43]; however, the authors used a steady-state model and considered the coefficients for charging and discharging processes as the same despite the difference in melting and solidification mechanisms. Referencing the same approach but changing the characteristics of ice and utilizing a dynamic model simulation, Henze and Krarti [44] developed a thermal storage model in EnergyPlus™ based on a storage tank with fixed capacity using ice as the phase change material. However, recent studies have increasingly focused on organic and inorganic PCMs due to several advantages over traditional ice/chilled water storage systems, such as the high latent heat. In addition, the PCM can be selected based on the operating temperature ranges, improving overall efficiency and system compatibility [45].

To overcome the limitations of existing active TES models restricted to ice/chilled water systems, this work develops generalized performance maps for predicting the thermal behavior of arbitrary PCMs, developing curve-fit correlations based on the *UA* values obtained from GRCM. Discharge and recharge rates are calculated following a similar logic to the empirical formulations used in the EnergyPlus™ ice storage model, but generalized for any PCM material. For the performance maps, the *UA* is modeled as a function of liquid fraction (x_{melt}) only, dynamically reflecting the changes in behavior during the phase change process. Separate sets of coefficients are generated for discharge and recharge due to the distinct dynamic thermal behaviors of each process. This methodology allows the performance maps to mimic the transient behavior of TES over the entire cycle in a faster and straightforward way, enabling accurate prediction of PCM-HX behavior under different conditions. The performance map equation that characterizes PCMs for TES integration to building simulation tools is shown in Eq.(4).

$$UA_{CF} = C_1 + C_2 x_{melt} + C_3 x_{melt}^2 + C_4 x_{melt}^3 + C_5 x_{melt}^4 + C_6 x_{melt}^5 \quad (4)$$

The UA_{CF} coefficients C_i are determined using linear regression, where the liquid fraction x_{melt} and UA_{CF} outputs from the GRCM at each time step serve as source data to the curve-fitting process. Given that the TES nominal storage capacity is fixed based on the PCM volume required to meet the building load during peak hours, the Q_{stor} term does not vary with time or operational conditions. As such, its inclusion does not affect the dynamic behavior or comparative analysis of the system under varying scenarios; thus, it was removed from the performance map equation. The resulting *UA* values from the regression model were evaluated against reference *UA* values calculated from the GRCM simulation, based on the LMTD method at each time step. The UA-LMTD data reduction procedure is summarized in Eqs. (5)-(7).

$$\dot{Q} = \dot{m} c_{p,water} (T_{water\_out} - T_{water\_in}) \quad (5)$$

$$LMTD = \frac{T_{water,in} - T_{water,out}}{\ln\left(\frac{T_{water,in} - T_{Nominal}}{T_{water,out} - T_{Nominal}}\right)} \quad (6)$$

$$UA_{GRCM} = \frac{\dot{Q}}{LMTD} \quad (7)$$

In which $\dot{Q}$ is the water heat transfer rate, $T_{Nominal}$ is the nominal PCM temperature, and $\dot{m}$ is the water mass flow rate.

2.3.2 Heat Pump System Level Performance Maps

The 5-ton (~17.5 kW) air-to-water HP system-level performance maps were developed based on transient component and system models using an in-house Modelica library [46]. The HP model includes two types of HX models: an outdoor microchannel HX (MCHX) and an indoor brazed plate HX (BPHX), each consisting of three types of volumes (CVs) which are segmented over the axial flow direction (Figure 4). A one-dimensional heat flow model was employed, neglecting axial conduction but capturing transient mass and energy balances for refrigerant and water CVs. For the water side, incompressible flow was assumed, while the air side adopted a quasi-steady approximation with uniform flow across the MCHX. Heat transfer was evaluated using bulk air and wall surface temperatures, with total sensible and latent heat flow determined from air and condensate enthalpies. These component models were used to construct performance maps that retain high fidelity while enabling computationally efficient system-level simulations. Additional model details can be found in Qiao et al. [46] and Othman et al. [47], [48].

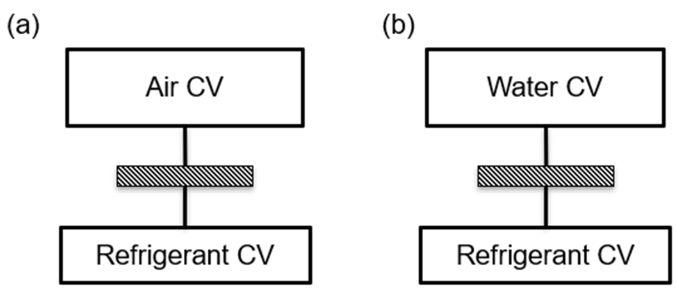

Figure 4. Representative Modelica model CV assembly: (a) MCHX, and (b) BPHX

To enable system-level evaluation of the proposed HP-TES integration, HP performance maps were developed under a wide range of outdoor and indoor boundary conditions. In cooling mode, the base HP performance maps (Eq. (8)) are expressed as a bi-quadratic function of indoor wet-bulb and outdoor dry-bulb temperatures, with fan and pump powers included according to the HP-TES operating mode. The maps were developed for an outdoor dry bulb temperature range of 18 – 50°C and glycol/water temperatures between −6°C – 14°C. Similarly, heating mode maps were developed for outdoor dry-bulb temperatures ranging from −35°C to 14°C and glycol/water temperatures between 20°C and 50°C (Eq. (9)). These temperature ranges were selected to cover a wide range of operations, including base and recharge operations for the A12 and A36 PCMs. When the air supply temperature fell below 32°C, auxiliary heating (COP = 1) was introduced [38].

$$\begin{bmatrix} \dot{Q}_{cap} \\ \dot{W}_{total} \end{bmatrix} = \begin{bmatrix} [A_1 ... A_6]_{\dot{Q}} \\ [A'_1 ... A'_6]_{\dot{W}} \end{bmatrix} f(T_{glycol}, T_{db,out}); \qquad COP_{cool} = \frac{\dot{Q}_{cap,cool}}{\dot{W}_{sys}} \tag{8}$$

$$\begin{bmatrix} \dot{Q}_{cap} \\ \dot{W}_{sys} \end{bmatrix} = \begin{bmatrix} [B_1 ... B_6]_{\dot{Q}} \\ [B'_1 ... B'_6]_{\dot{W}} \end{bmatrix} f(T_{glycol}, T_{db,out}) \qquad COP_{heat} = \frac{\dot{Q}_{cap,heating} + \dot{Q}_{aux}}{\dot{W}_{sys} + \dot{Q}_{aux}} \tag{9}$$

The coefficients A and B from Eqs.(8)-(9) characterize HP capacity and power requirement for PCM recharge. In discharge mode, the PCM-TES operates independently based on the GRCM performance maps until fully discharged. By combining HP and PCM-HX performance maps, the framework ensures computationally efficient evaluation of HP-TES operation across representative building conditions and climate zones.

2.4 Case Study: Building Simulation with HP-TES

To demonstrate the feasibility of the proposed integrated methodology, a DOE prototype small office building was conditioned using a dual-mode HP-TES employing two separate PCM-HXs, one for cooling and one for heating, allowing for the selection of PCM nominal temperature that are well aligned with outdoor conditions for each season. The HP-TES can flexibly switch operation, providing space conditioning using the base HP and/or TES (discharge and recharge) depending on the defined control strategy, e.g., a rule-based control algorithm where TES is only used during utility peak TOU hours for the target locations [49], [50] or according to a model-predictive control framework based on PCM utilization (SOC). The schematic for the HP-TES developed for heating and cooling applications is shown in Figure 5, illustrating base operation (Figure 5a), TES discharge (Figure 5b), and recharge (Figure 5c). During peak periods, to shave electricity, the HP system is turned off and the thermal battery is activated to meet the required building load through the hydronic loop. In the recharge mode, once the PCM is fully depleted, the base HP system is utilized to meet the building load while the PCM is restored to its fully charged state.

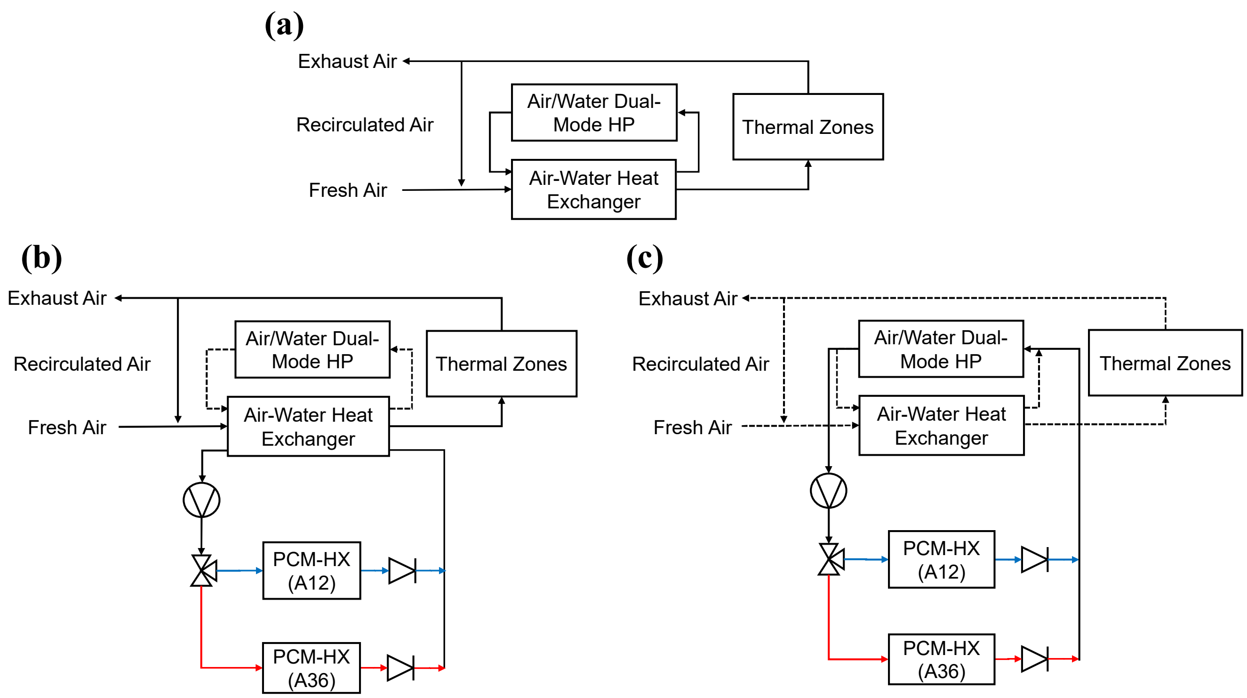

Figure 5. HP-TES system schematic diagram: (a) base operation, (b) discharge operation, and (c) recharge operation

The base system consists of an air-to-water heat pump equipped with an outdoor MCHX, a single-speed compressor, and BPHX, as shown in Figure 6. The BPHX connects either to the indoor air-to-water coil or to the PCM-HXs during TES recharge. In cooling mode, the BPHX solidifies the A12 PCM, while in heating mode, it melts the A36 PCM. A 45% propylene glycol/water mixture is used as the heat transfer fluid in the hydronic loop to provide freeze protection, particularly during heating season charging events when evaporating temperatures fall below freezing. The refrigerant R410A is used for heat pump operation in both heating and cooling modes.

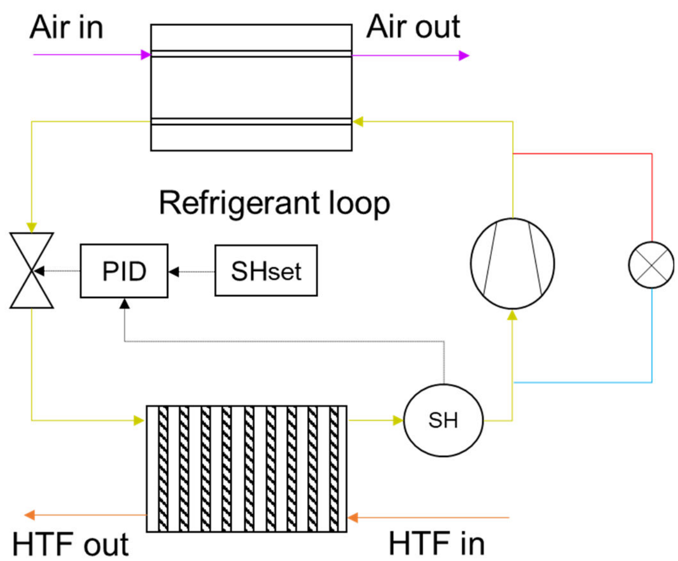

Figure 6. Base heat pump schematic

2.5 Modelica Buildings Library Interface and Performance Maps Integration for Spawn of EnergyPlus™

Figure 7 shows the Dymola interface of the HP-TES system, incorporating the PCM-HX integrated HP system, Spawn of EnergyPlus™, and the DOE small office prototype [34], [35], [37]. The air-to-water HP-TES system and controls consist of the PCM-HX unit model, in which a water/glycol mixture is circulated at a controlled mass flow rate, while the building block represents the thermal zones (DOE small-office building) that interact with the HX to regulate indoor conditions. The air-to-water HX is operated with 95% recirculated air and 5% fresh intake, with sensors monitoring supply air temperature and flow rates. Spawn of EnergyPlus™ provides input data files and weather data for the selected climate zones, enabling building-level dynamic load evaluation.

While other control strategies can be utilized with HP-TES systems, a rule-based control strategy was considered for demonstration of the methodology, given its robustness in predicting load-shift and cost savings [51]. The HP-TES control logic was implemented based on the TOU electricity pricing schedules of 3 PM to 9 PM in Minnesota [49] and 12 PM to 9 PM in Florida [50]. These cities were selected because their climate conditions impose high space conditioning demands, resulting in more frequent HP-TES discharge/recharge cycles. The HP-TES controller requires two external inputs: the daily operating hours and the thermostat setpoints. The thermostat setpoints regulate indoor temperature and HVAC activation in response to building thermal loads, while the TOU hours determine when TES discharge or recharge is enabled. Discharge occurs during on-peak periods when the PCM SOC is between 95% to 5%. Once the liquid fraction drops below 5%, the control signal shifts the operation to recharge, which occurs during off-peak (nighttime) periods to minimize energy consumption, i.e., the coolest nighttime hours for cooling mode (latest nocturnal hours) and the warmest for heating (earliest nocturnal hours). Once the recharge is completed (SOC ≥ 95%), the system resets, and the discharge mode is possible for the next TOU cycle.

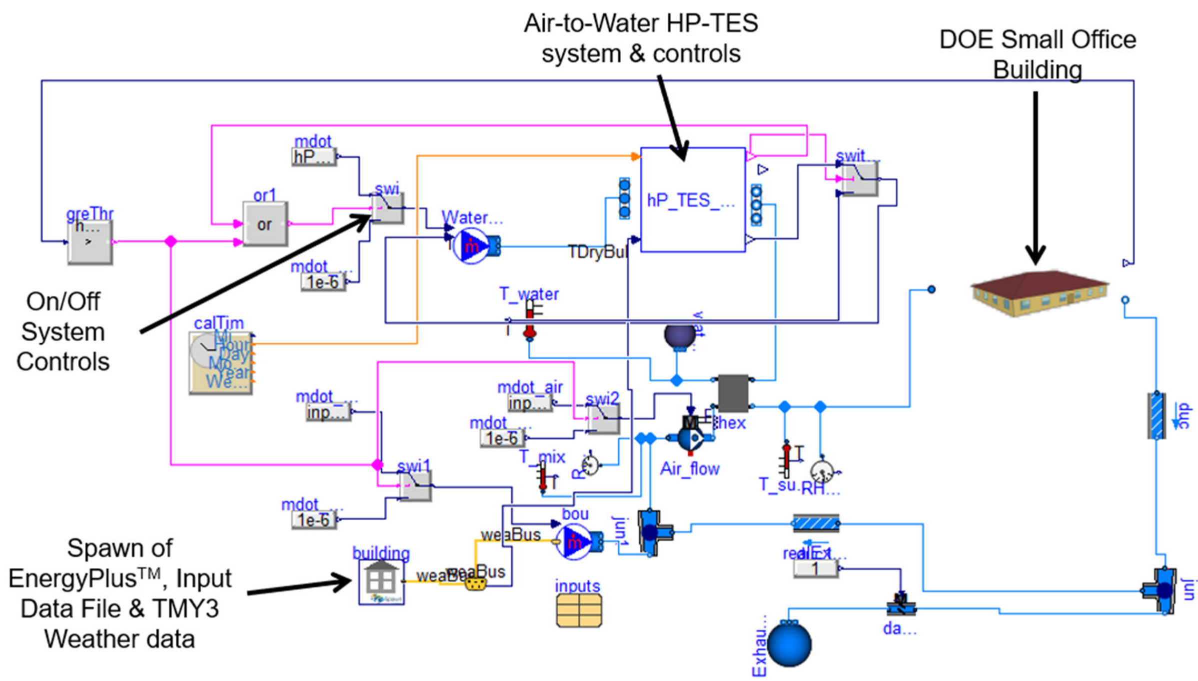

Figure 7. Dymola interface with HP-TES system, DOE small office prototype building, and Spawn of EnergyPlus™ [34]

3. Results and Discussion

3.1 PCM-HX Performance Map Verification

To ensure the applicability of the proposed methodology, it is required to first verify its accuracy in reproducing the system dynamics in a shorter time. The verification involves two comparisons: (i) the performance maps with PCM-HX GRCM simulation data and (ii) the Modelica curve-fit component to PCM-HX GRCM data.

3.1.1 PCM-HX Performance Prediction

The TES performance was first predicted using the GRCM, and the outputs were employed to construct the PCM-HX performance maps in both heating and cooling modes under representative HTF operating conditions, i.e., the inlet temperature of the propylene glycol/water mixture was set to 19°C during cooling mode discharge and 5°C during cooling mode recharge. For heating, the inlet temperatures were defined as 27°C (discharge) and 45°C (recharge). A constant thermal battery mass flow rate was defined as 0.78 kg/s across all simulations. The resulting liquid fraction outputs obtained from GRCM (Figure 8a, b) were used to generate the performance maps to characterize the transient behavior of the PCM-HX unit. The fitted coefficient values for discharge and recharge processes in both cooling and heating modes are showed in Table 4.

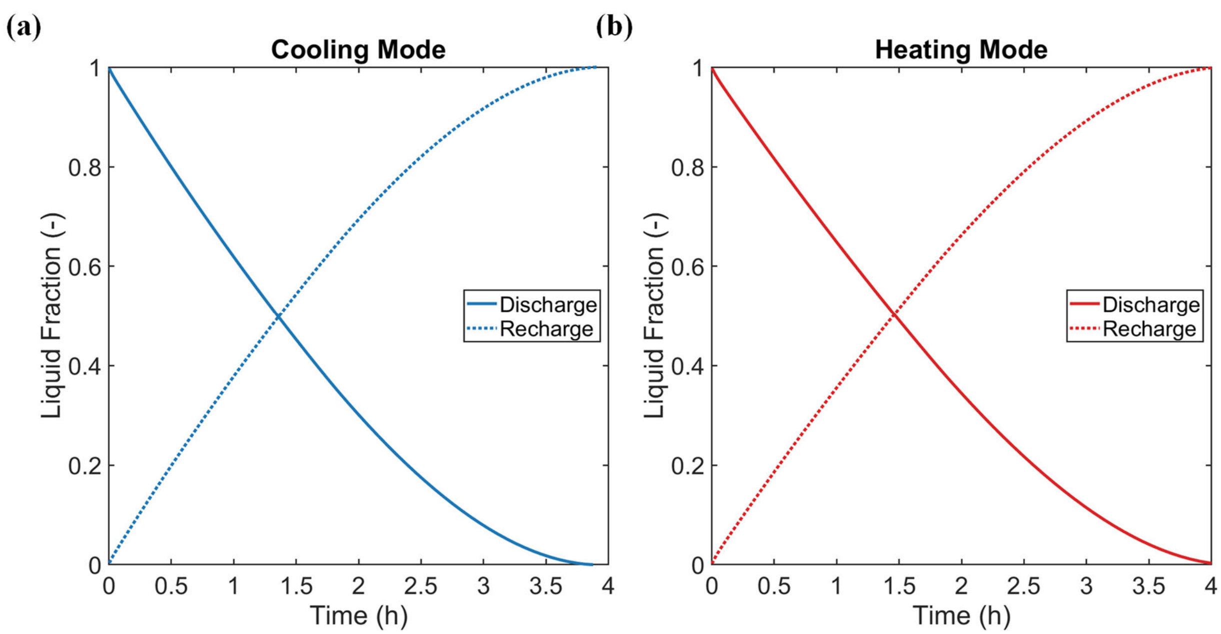

Figure 8. PCM-HX average liquid fraction during heating and cooling mode recharge and discharge operation

Table 4. *UA* coefficients for PCM-HX cooling and heating mode performance maps

Coefficients	Cooling Mode		Heating Mode	
	Discharge	Recharge	Discharge	Recharge
C1	9.65E+03	3.39E+02	4.05E+02	8.06E+03
C2	-2.78E+04	1.56E+04	1.56E+04	-1.59E+04
C3	7.49E+04	-3.72E+04	-3.00E+04	3.93E+04

C4	-1.26E+05	7.25E+04	4.65E+04	-6.68E+04
C5	1.07E+05	-7.72E+04	-4.33E+04	5.69E+04
C6	-3.79E+04	3.53E+04	1.86E+04	-2.11E+04

To verify the accuracy of the performance maps, Figure 9 shows a comparison of the curve-fit model predicted *UA* and GRCM *UA* for discharge and recharge in cooling mode. The heating mode results were very similar, and thus are not presented herein. The results demonstrate that the performance maps closely reproduce the GRCM-predicted *UA*, with an average absolute percentage error in the range of 2.0 - 4.6% and a maximum percentage error of 7.7%, which was observed during the cooling mode shutdown process. The deviations between the curve-fit and GRCM results increase when the PCM approaches complete solidification ($x_{melt} \sim 0.0$) or melting ($x_{melt} \sim 1.0$), as the curve-fit was developed primarily to represent the transient behavior during the phase change process (i.e., highest energy stored). Therefore, the performance maps are less accurate during start-up and shut-down operations. Nevertheless, the *UA* predictions from the curve-fit equations were very good and thus considered acceptable for full system simulation.

Table 5 shows the root mean square error (RMSE) and coefficient of variation of root mean square error (CV(RMSE)) for the performance maps compared to GRCM results. The low RMSE values in both heating and cooling mode indicate minor deviations between the performance maps and GRCM-predicted *UA*, corresponding to less than 3% of the *UA* magnitude in each case. These results demonstrate that the performance maps accurately reproduce the transient PCM behavior predicted by the GRCM.

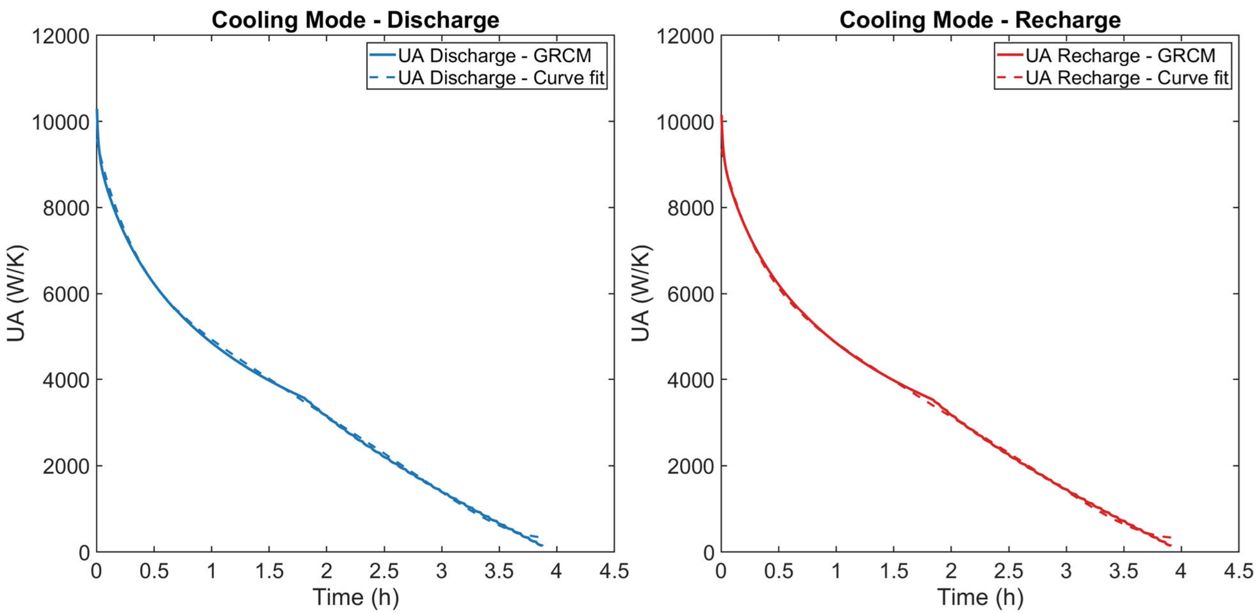

Figure 9. Cooling mode verification: Performance maps vs. full GRCM simulations

Table 5. RMSE and CV(RMSE) of the performance maps compared to the GRCM model

	Cooling Mode		**Heating Mode**	
	Discharge	Recharge	Discharge	Recharge
RMSE (W/K)	71.0	63.1	61.4	63.1
CV (RMSE) (%)	2.1	1.8	1.8	1.8

3.1.2 Modelica Component Verification

Figure 10 presents a comparison of the full GRCM prediction and the performance map-based PCM-HX component model simulated in Modelica, highlighting the heat transfer rate vs. SOC for all four operating modes (cooling-discharge; cooling-recharge; heating-discharge; heating-recharge). Overall, there is a good agreement between the Modelica performance map-based PCM-HX component and GRCM, with an average absolute percentage error ranging from 2.3% to 3.6%, and a maximum percentage error of 10.9% observed during shut-down of cooling mode recharge. The discrepancy between the two models is likely due to the curve-fit being less accurate during start-up and shut-down operations, as the performance maps methodology was developed to represent the phase-change process only (i.e., *SOC* from 5% – 95%). Nevertheless, the performance maps model successfully reproduces the TES behavior in Modelica, demonstrating strong predictive capability. The RMSE ranges from 0.3 to 0.5, with a maximum value of 1.0 for the heat transfer prediction during recharge in cooling mode.

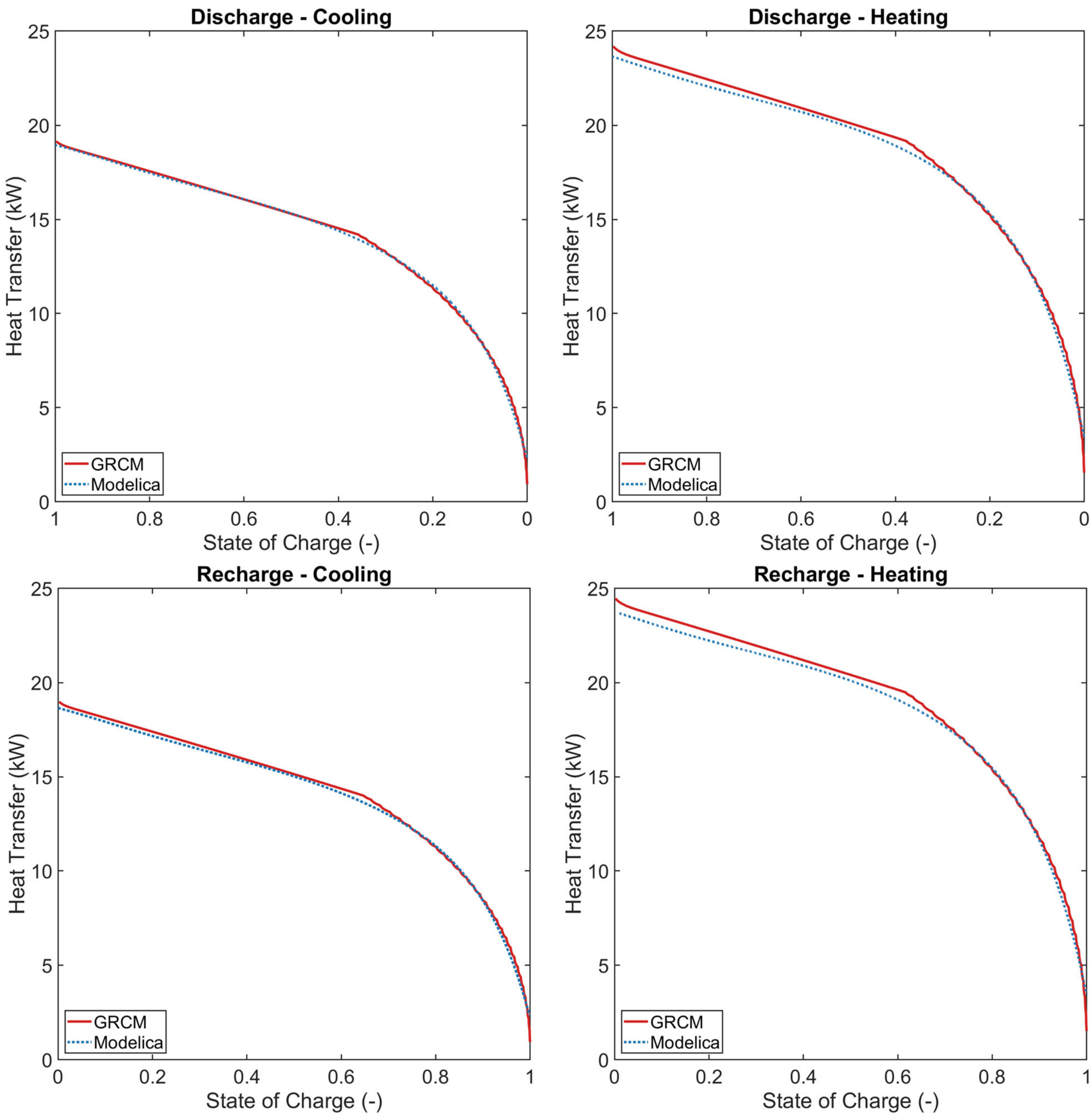

Figure 10. Modelica PCM-HX curve-fit model verification vs. full GRCM simulation

A key advantage of employing the proposed performance map methodology lies in the considerable reduction in simulation time, which is critical for design optimization, PCM parametric studies and development of optimized control strategies to maximize load-shifting and energy savings. For instance, simulating a 4.5-hour discharging or recharging process using the performance map-based PCM-HX in Modelica was found to be at least 1800 times faster compared to full GRCM simulations on the same computer. Therefore, the adoption of performance maps provides the scalability and computational efficiency needed for coupling with large-scale, complex building energy simulations and control strategies, enabling rapid full-year simulations without compromising component-level prediction accuracy.

3.2 Multi-Day HP-TES System-Level Simulations

A set of multi-day simulations were conducted using the TES performance maps to highlight that the methodology can enable system-level performance assessments. The simulations were carried out over four typical meteorological days [33] (midnight to midnight) for January 2nd - 5th in International Falls, MN (heating) and July 4th - 7th in Tampa, FL (cooling), covering multiple periods of TES discharge, recharge, and system cycling in both locations. During TOU hours, the system shifts from base HP operation to TES discharge until the PCM storage is fully exhausted, then reverts to base HP or recharges during off-peak periods or when the PCM is depleted, thereby mitigating peak electricity demand.

3.2.1 Multi-Day Simulation of HP-TES in Tampa, FL

Figure 11 shows a multi-day simulation for cooling mode in Tampa, FL, comparing base HP operation with the integrated HP-TES system. In the base plot, the gray line represents the power consumption along with the indoor setpoint and outdoor dry bulb temperatures. In the HP-TES plot (bottom), the water/glycol inlet and outlet temperatures are also shown to identify the discharge and recharge operation times. Discharge operation initiates when compressor power is off and the water/glycol temperature is above the PCM nominal temperature (marked as D). When PCM is fully depleted, the recharge initiates, identified by a drop in the water/glycol temperature (marked as R), with the compressor operating continuously to provide both recharge and building load. The indoor temperature is effectively maintained at 24°C ± 1 K, with on-off cycling intervals based on thermostat setpoint control. In addition, it is possible to observe the rule-based TOU control strategy, when the TES activates during peak hours until it is fully depleted, followed by recharge operation during off-peak periods, i.e., the coolest nighttime hours. Based on the power consumption profile, the TES reduces reliance on the HP during discharge, decreasing peak-hour energy demand by 17.4% over the simulation period.

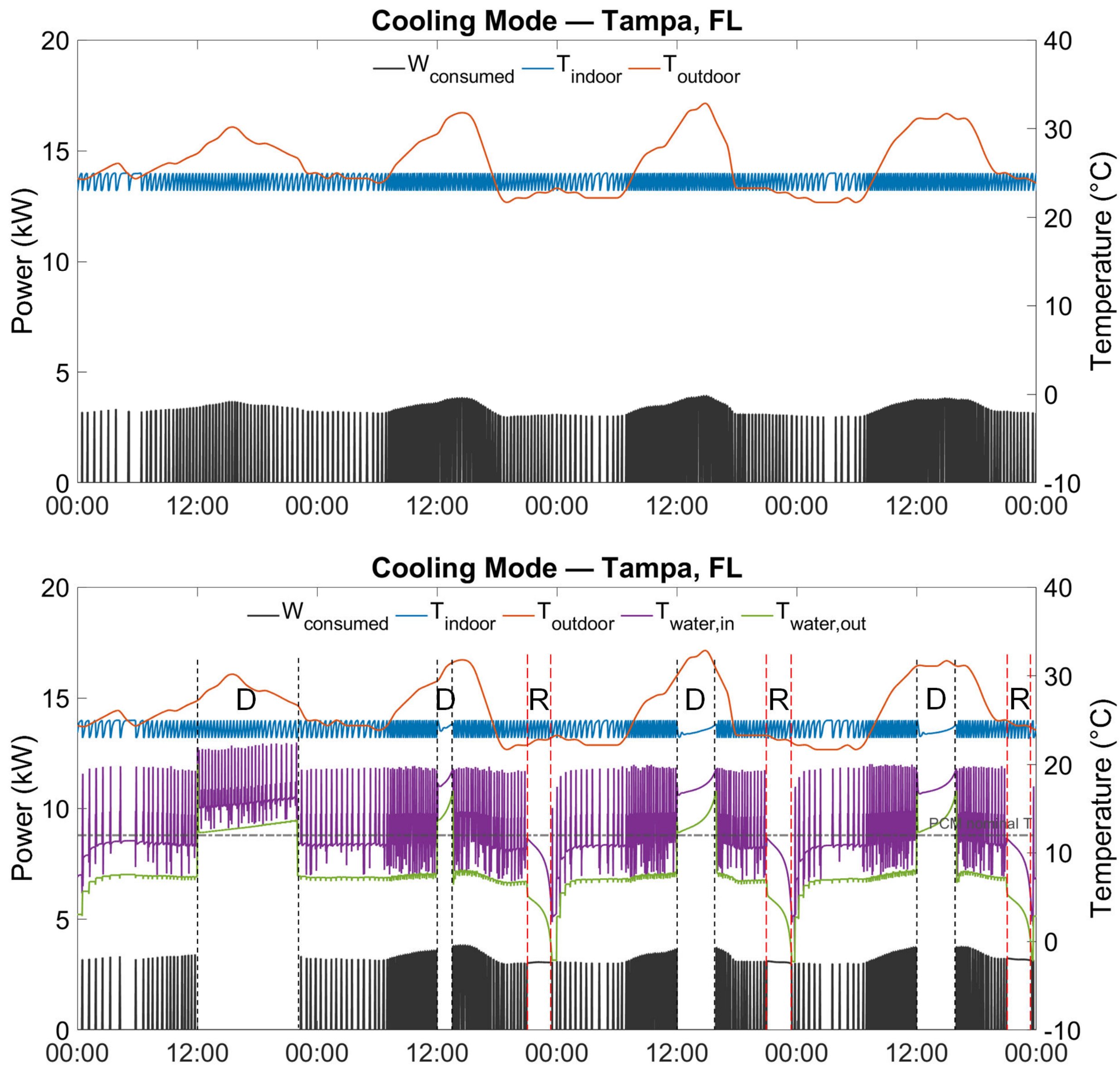

Figure 11. (Top) base HP-operation; (bottom) HP-TES operation in Tampa, FL during cooling mode

3.2.2 Multi-Day Simulation of HP-TES in International Falls, MN

Figure 12 shows the multi-day simulation for heating mode in International Falls, MN, again comparing base HP operation with the integrated HP-TES system. In extreme cold climates, the HP efficiency significantly drop due to increased pressure ratio across the compressor, reducing heating capacity. When the outdoor dry bulb temperature is extremely low, outside the HP operating envelope, the base HP is not able to meet the required system capacity without auxiliary heating [52]. This combined effect of reduced heating capacity and increased reliance on backup heating lowers the overall system efficiency. Under these extreme conditions, regions like

International Falls showcase the benefits of integrating TES with HP systems. The integration with the TES system reduces the need for backup heating during peak hours, increasing overall system efficiency (Figure 13). During this simulation period, the total backup heater energy consumption was reduced by 87.4%, resulting in a significant on-peak demand reduction during extreme cold events. As a result, the total energy consumption in International Falls decreased by 62.2%, mainly driven by the reduced operation of the electric backup heater.

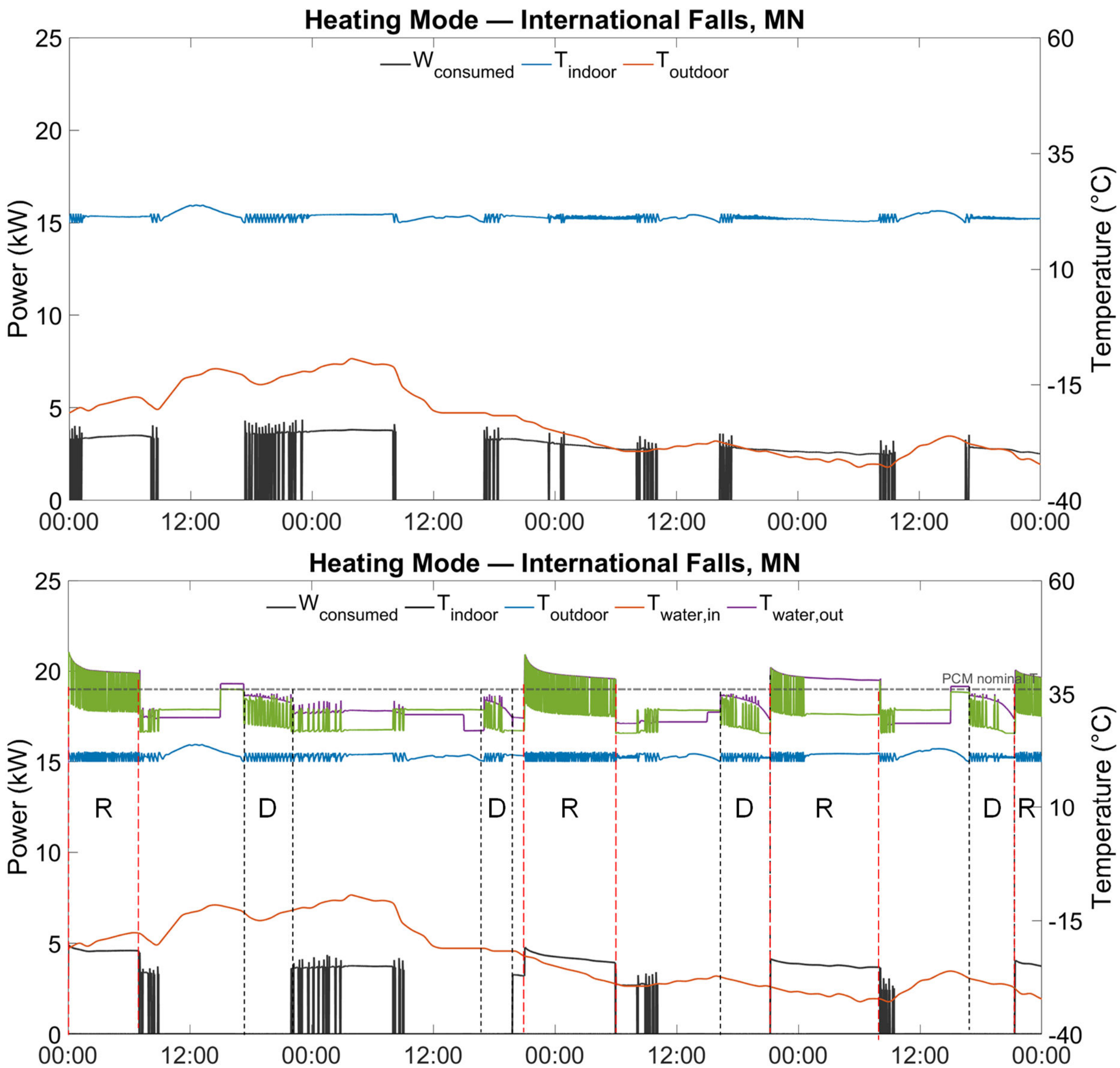

Figure 12. (Top) base HP-operation; (bottom) HP-TES operation in International Falls, MN during heating mode

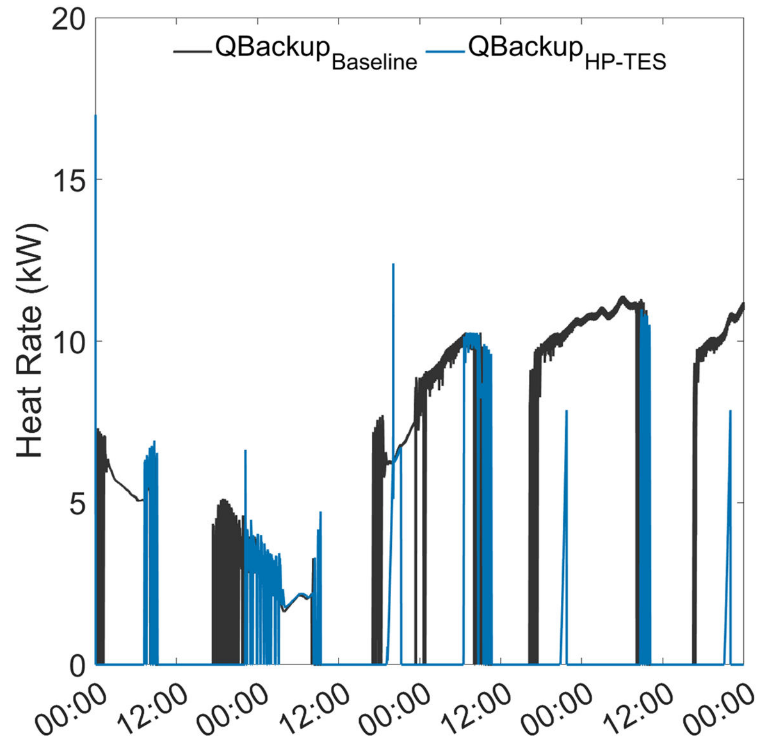

Figure 13. Backup heating requirement for base HP and HP-TES operation

4. Conclusion

This paper presents a computationally efficient framework for simulating building energy systems integrated with LHTES. In this approach, PCM-HXs are represented using performance maps constructed using source data from a generalized PCM-HX modeling tool, which are then integrated into HVAC system models as curve-fit components and simulated in Modelica with building loads computed using Spawn of EnergyPlus™ to determine the impact of TES-integrated HVAC systems on full building energy consumption. The performance maps showed excellent agreement with detailed PCM-HX component simulations, with average absolute percentage errors within 2-4%. When implemented as a dynamic component model in Modelica, the performance maps characterized PCM-HX behavior with excellent accuracy while achieving at least 1800 times speedup compared to full GRCM simulations, which are themselves at least 1000 times faster than full CFD runs. The performance map methodology was further verified by considering multi-day simulation case studies for dual-mode HP-TES systems in two representative ASHRAE climate zones: Tampa, FL (cooling mode) and International Falls, MN (heating mode). In both cases, the HP-TES system reduced on-peak demand, by up to 17.4% in Tampa, FL, and 62.2% in International Falls, MN, mainly due to the HP-TES reducing the need for backup heating during extreme cold events. The PCM performance maps provide a simplified yet accurate representation of TES behavior, eliminating the need for detailed enthalpy formulations in Modelica and reducing computational cost without compromising accuracy. Overall, the proposed HP-TES performance maps methodology provides a robust and accurate modeling framework for PCM-HXs with any type of PCM material in a component and system level integration, opening new opportunities for design optimization, advanced control strategy development, and parametric analysis of TES configurations in a cost-effective and computationally efficient manner. Future efforts should extend the proposed approach to demonstrate the feasibility in more complex HP-TES configurations and control strategies, including the generation of HP-TES maps that account for variable speed components and direct integration of TES in vapor compression cycle.

Acknowledgments

This material is based upon work supported by the U.S. Department of Energy's Office of Energy Efficiency and Renewable Energy (EERE) under the Building Technologies Office (BTO) Award Number DE-EE0009158. The views expressed herein do not necessarily represent the views of the U.S. Department of Energy or the United States Government. This work was also supported in part by the Modeling & Optimization Consortium at the Center for Environmental Energy Engineering at the University of Maryland.

Appendix A. Heat Pump System Modeling and Performance Map Development

System-level transient models were constructed using an in-house Modelica library from Qiao et al [46] to assess system performance under different air and glycol operating conditions. The outdoor air temperatures considered was -35°C and 14°C in heating mode and 18°C to 50°C in cooling mode, while the selected water/glycol temperatures were in accordance with AHRI Standards 550/590 [53]. The properties of the 45% propylene glycol/water mixture were obtained from the Modelica Standard Library [54]. The system performance for both cooling and heating modes was determined using Eq.(10).

$$COP = \frac{\dot{Q}_{cool}}{\dot{W}_{comp} + \dot{W}_{pump} + \dot{W}_{fan}} \tag{10}$$

The COPs, capacities, and power demand in both cooling and heating modes were determined across the different air and water-glycol temperature ranges. Figure A1 shows the simulated COPs in both cooling and heating modes for water/brine inlet temperatures of 10°C (50°F) and 25°C (77°F). In heating mode, multiple correlations were developed based on the outdoor dry-bulb temperature window. Figure A1(b) shows an example of the simulated COP based on an outdoor dry-bulb operating window from -15°C to 14°C.

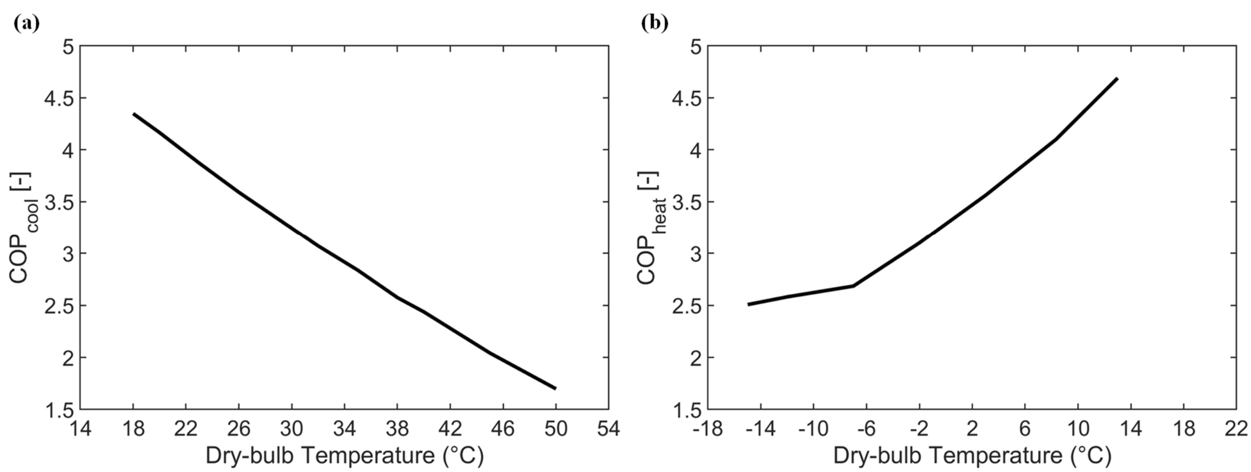

Figure A1. Base HP system COP based on outdoor dry-bulb temperature in (a) cooling mode (T_{glycol} = 10 °C), and (b) heating mode (T_{glycol} = 25 °C)

The HP performance maps utilize a bi-quadratic functional form accounting for both the 45% propylene glycol/water mixture and outdoor ambient conditions. The maps were obtained for both system capacity and total power demand, combining compressor, pump, and fan powers. The equation form is shown in Eqs. (11)-(12), where different coefficients were required for heating and cooling mode due to different operating conditions in the vapor compression cycles. The maps were generated for use in base, discharge, and recharge modes.

$$\dot{Q}_{cap} = A_1 + A_2 T_{db,out} + A_3 T_{glycol} + A_4 (T_{db,out})^2 + A_5 (T_{db,out})(T_{glycol}) + A_6 (T_{glycol})^2 \quad (11)$$

$$\dot{W}_{sys} = A'_1 + A'_2 T_{db,out} + A'_3 T_{glycol} + A'_4 (T_{db,out})^2 + A'_5 (T_{db,out})(T_{glycol}) + A'_6 (T_{glycol})^2 \quad (12)$$

The HP maps were generated in cooling and heating modes, respectively, using data generated by the Modelica model. Example coefficients are presented in Table A1, along with the coefficient of determination (R^2) and RMSE.

Table A1: Coefficients for HP cooling and heating mode performance maps

Coefficients	Cooling Mode		Heating Mode	
	Capacity	Power	Capacity	Power
A_1	1.48E+04	1.18E+03	1.56E+04	−1.31E+03
A_2	−6.87E+01	4.02E+01	4.44E+02	1.20E+00
A_3	5.33E+02	1.19E+02	6.46E+01	2.41E+02
A_4	−1.07E+00	9.92E−01	2.85E+00	−1.23E+00
A_5	−3.52E+00	−1.28E+00	−7.19E−01	−3.18E−02
A_6	1.10E+00	−4.02E+00	−1.66E+00	−1.92E+00
R^2	0.999	0.996	0.988	0.934
RMSE	0.05	0.07	0.06	0.02

Verifications were conducted for the HP maps on varying outdoor air temperatures from -8°C to 8°C in heating mode, and 10°C to 30°C in cooling mode. The water/glycol conditions corresponded to inlet and outlet conditions for PCM recharge temperatures in cooling and heating modes. The base HP transient model, coupled with the TES performance maps, was simulated under recharge conditions and compared with the base HP maps in both modes, with maximum deviations of 3%, as can be seen in Figure A2.

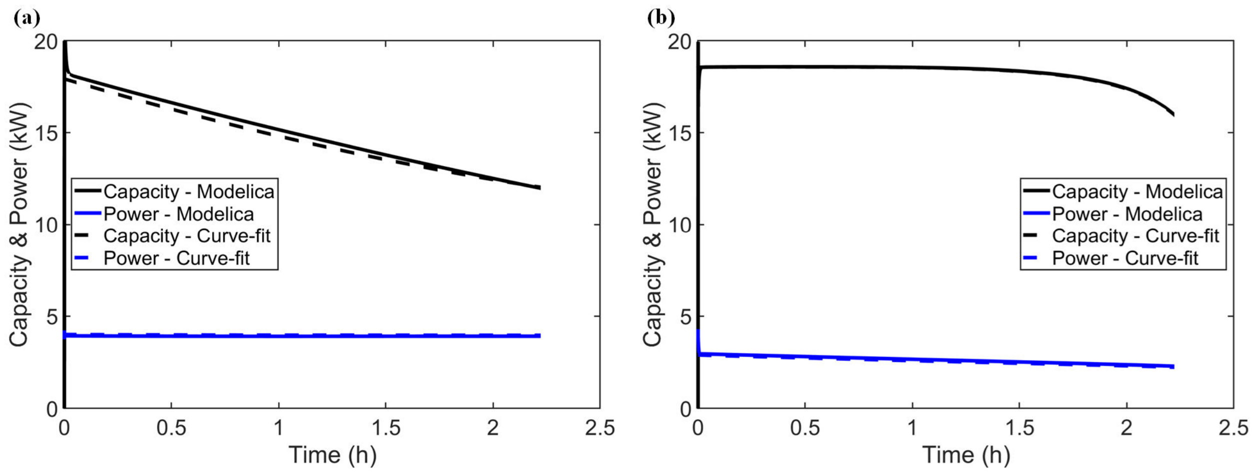

Figure A2. Capacity and Power comparison between Modelica simulation and HP performance maps: (left) heating mode and (right) cooling mode

References

[1] S. Zhang, P. Ocłoń, J. J. Klemeš, P. Michorczyk, K. Pielichowska, and K. Pielichowski, "Renewable energy systems for building heating, cooling and electricity production with thermal energy storage," *Renew. Sustain. Energy Rev.*, vol. 165, p. 112560, Sept. 2022, doi: 10.1016/j.rser.2022.112560.

[2] Energy Information Administration - EIA, "Monthly Energy Review," Dec. 2024.

[3] M. Ma, N. Zhou, W. Feng, and J. Yan, "Challenges and opportunities in the global net-zero building sector," *Cell Rep. Sustain.*, vol. 1, no. 8, p. 100154, Aug. 2024, doi: 10.1016/j.crsus.2024.100154.

[4] International Energy Agency (IEA), "Net Zero by 2050 - A Roadmap for the Global Energy Sector".

[5] U.S. Energy Information Administration (EIA), "Commercial Buildings Energy Consumption Survey final results," U.S. Energy Information Administration, 2018.

[6] M. Uddin, M. F. Romlie, M. F. Abdullah, S. Abd Halim, A. H. Abu Bakar, and T. Chia Kwang, "A review on peak load shaving strategies," *Renew. Sustain. Energy Rev.*, vol. 82, pp. 3323–3332, Feb. 2018, doi: 10.1016/j.rser.2017.10.056.

[7] F. Torbarina, K. Lenic, A. Trp, and M. Kirincic, "Parametric analysis of system performance and cost of heating systems with heat pump and latent thermal energy storage," *Appl. Therm. Eng.*, vol. 252, p. 123717, Sept. 2024, doi: 10.1016/j.applthermaleng.2024.123717.

[8] J. Hirschey, Z. Li, K. R. Gluesenkamp, T. J. LaClair, and S. Graham, "Demand reduction and energy saving potential of thermal energy storage integrated heat pumps," *Int. J. Refrig.*, vol. 148, pp. 179–192, Apr. 2023, doi: 10.1016/j.ijrefrig.2023.01.026.

[9] S. Bourne and A. Novoselac, "Improved performance in tube-encapsulated phase change thermal energy stores for HVAC applications," *Build. Environ.*, vol. 98, pp. 133–144, Mar. 2016, doi: 10.1016/j.buildenv.2015.12.023.

[10] H. Togun *et al.*, "A critical review on phase change materials (PCM) based heat exchanger: Different hybrid techniques for the enhancement," *J. Energy Storage*, vol. 79, p. 109840, Feb. 2024, doi: 10.1016/j.est.2023.109840.

[11] R. A. Kishore, M. V. A. Bianchi, C. Booten, J. Vidal, and R. Jackson, "Optimizing PCM-integrated walls for potential energy savings in U.S. Buildings," *Energy Build.*, vol. 226, p. 110355, Nov. 2020, doi: 10.1016/j.enbuild.2020.110355.

[12] V. Piroozmand and R. Ahmadi, "Enhancement of PCMs performance using nano-particles in horizontal triple-series shell-and-tube heat exchangers: A numerical study," *J. Energy Storage*, vol. 85, no. December 2023, p. 111057, 2024, doi: 10.1016/j.est.2024.111057.

[13] R. Huang, A. Mahvi, N. James, E. Kozubal, and J. Woods, "Evaluation of phase change thermal storage in a cascade heat pump," *Appl. Energy*, vol. 359, p. 122654, Apr. 2024, doi: 10.1016/j.apenergy.2024.122654.

[14] R. Du, M. Wu, S. Wang, S. Wu, R. Wang, and T. Li, "Integrated heat pump with phase change materials for space heating," *Renew. Sustain. Energy Rev.*, vol. 203, p. 114769, Oct. 2024, doi: 10.1016/j.rser.2024.114769.

[15] J. Sun, K. Nawaz, J. Rendall, A. Elatar, and J. Brechtl, "Heat pump water heater enhanced with phase change materials thermal energy storage: Modeling study," *Int. Commun. Heat Mass Transf.*, vol. 146, p. 106917, July 2023, doi: 10.1016/j.icheatmasstransfer.2023.106917.

[16] Y. Zhang, M. V. Bozorg, J. F. Torres, Y. Zhao, and X. Wang, "Dynamic melting of encapsulated PCM in various geometries driven by natural convection of surrounding air: A modelling-based parametric study," *J. Energy Storage*, vol. 48, no. January, p. 103975, 2022, doi: 10.1016/j.est.2022.103975.

[17] A. König-Haagen, M. Faden, and G. Diarce, "A CFD results-based reduced-order model for latent heat thermal energy storage systems with macro-encapsulated PCM," *J. Energy Storage*, vol. 73, no. May, 2023, doi: 10.1016/j.est.2023.109235.

[18] D. Bacellar, T. Alam, J. Ling, and V. Aute, "A Study on Computational Cost Reduction of Simulations of Phase-Change Material (PCM) Embedded Heat Exchangers," *18th Int. Refrig. Air Cond. Conf. Purdue*, pp. 1–9, 2021.

[19] Y. Li, Z. O'Neill, L. Zhang, J. Chen, P. Im, and J. DeGraw, "Grey-box modeling and application for building energy simulations - A critical review," *Renew. Sustain. Energy Rev.*, vol. 146, p. 111174, Aug. 2021, doi: 10.1016/j.rser.2021.111174.

[20] R. Kramer, J. Van Schijndel, and H. Schellen, "Simplified thermal and hygric building models: A literature review," *Front. Archit. Res.*, vol. 1, no. 4, pp. 318–325, Dec. 2012, doi: 10.1016/j.foar.2012.09.001.

[21] J. Gao, T. Yan, T. Xu, Z. Ling, G. Wei, and X. Xu, "Development and experiment validation of variable-resistance-variable-capacitance dynamic simplified thermal models for shape-stabilized phase change material slab," *Appl. Therm. Eng.*, vol. 146, pp. 364–375, Jan. 2019, doi: 10.1016/j.applthermaleng.2018.09.124.

[22] H. Neumann, S. Gamisch, and S. Gschwander, "Comparison of RC-model and FEM-model for a PCM-plate storage including free convection," *Appl. Therm. Eng.*, vol. 196, no. September 2020, p. 117232, 2021, doi: 10.1016/j.applthermaleng.2021.117232.

[23] T. Alam, D. Bacellar, J. Ling, and V. Aute, "Development and Validation of Resistance-Capacitance Model for Phase Change Material Embedded in Porous Media," *Intersoc. Conf. Therm. Thermomechanical Phenom. Electron. Syst. ITHERM*, vol. 2022-May, no. 2011, pp. 1–10, 2022, doi: 10.1109/iTherm54085.2022.9899532.

[24] H. Wan, X. Xu, T. Xu, K. K. R. Yuen, and G. Huang, "Development of a quasi-2D variable resistance–capacitance model for tube-encapsulated phase change material storage tanks," *Appl. Therm. Eng.*, vol. 214, p. 118868, Sept. 2022, doi: 10.1016/j.applthermaleng.2022.118868.

[25] J. Yin, S. Wang, X. Hou, Z. Wang, M. Ye, and Y. Xing, "Transient prediction model of finned tube energy storage system based on thermal network," *Appl. Energy*, vol. 336, p. 120861, Apr. 2023, doi: 10.1016/j.apenergy.2023.120861.

[26] M. Menezes, J. Tancabel, D. Bacellar, and V. Aute, "Development & Experimental Validation of a Generalized Resistance-Capacitance Model for Numerical Simulation of Phase-Change Material Embedded Heat Exchangers," *20th Int. Refrig. Air Cond. Conf.*, pp. 1–10, 2024.

[27] X. Wang, S. Tian, J. Ren, X. Jin, X. Zhou, and X. Shi, "A novel resistance-capacitance model for evaluating urban building energy loads considering construction boundary heterogeneity," *Appl. Energy*, vol. 361, p. 122896, May 2024, doi: 10.1016/j.apenergy.2024.122896.

[28] R. Kamal, F. Moloney, C. Wickramaratne, A. Narasimhan, and D. Y. Goswami, "Strategic control and cost optimization of thermal energy storage in buildings using EnergyPlus," *Appl. Energy*, vol. 246, pp. 77–90, July 2019, doi: 10.1016/j.apenergy.2019.04.017.

[29] J. Marchante-Avellaneda, E. Navarro-Peris, and Y. Song, "Development of map-based models for the performance characterization in a new prototype of Dual Source Heat Pump," *Appl. Therm. Eng.*, vol. 236, p. 121743, Jan. 2024, doi: 10.1016/j.applthermaleng.2023.121743.

[30] P. Ihm, M. Krarti, and G. P. Henze, "Development of a thermal energy storage model for EnergyPlus," *Energy Build.*, vol. 36, no. 8, pp. 807–814, Aug. 2004, doi: 10.1016/j.enbuild.2004.01.021.

[31] R. Z. Homod *et al.*, "Flattening power curves in smart buildings: Deep reinforcement learning for enhancing chiller performance and binary phase change materials," *J. Energy Storage*, vol. 140, p. 119163, Dec. 2025, doi: 10.1016/j.est.2025.119163.

[32] R. Z. Homod *et al.*, "Smart buildings using compact heat pipes with nanofluid in PCM for energy saving via deep clustering of multi-agent," *J. Build. Eng.*, vol. 112, p. 113771, Oct. 2025, doi: 10.1016/j.jobe.2025.113771.

[33] S. Wilcox and W. Marion, "Users Manual for TMY3 Data Sets (Revised)," National Renewable Energy Lab. (NREL), Golden, CO (United States), NREL/TP-581-43156, May 2008. doi: 10.2172/928611.

[34] M. Wetter, K. Benne, H. Tummescheit, and C. Winther, "Spawn: coupling Modelica Buildings Library and EnergyPlus to enable new energy system and control applications," *J. Build. Perform. Simul.*, vol. 17, no. 2, pp. 274–292, Mar. 2024, doi: 10.1080/19401493.2023.2266414.

[35] M. Wetter, W. Zuo, T. S. Nouidui, and X. Pang, "Modelica Buildings library," *J. Build. Perform. Simul.*, vol. 7, no. 4, pp. 253–270, July 2014, doi: 10.1080/19401493.2013.765506.

[36] https://www.3ds.com/products/catia/dymola, *Dymola*. Modelica. Dassault Systèmes.

[37] Dept. of Energy Building Technologies Office, "Prototype Building Models | Building Energy Codes Program," 2022, Accessed: Nov. 03, 2022. [Online]. Available: https://www.energycodes.gov/prototype-building-models

[38] "Standard 90.1." Accessed: June 29, 2025. [Online]. Available: https://www.ashrae.org/technical-resources/bookstore/standard-90-1

[39] W. Delgado-Diaz, A. Stamatiou, S. Maranda, R. Waser, and J. Worlitschek, "Comparison of Heat Transfer Enhancement Techniques in Latent Heat Storage," *Appl. Sci.*, vol. 10, no. 16, p. 5519, Aug. 2020, doi: 10.3390/app10165519.

[40] Churchill, "A comprehensive correlating equation for laminar, assisting, forced and free convection," *Am. Inst. Chem. Eng. J.*, vol. 23, no. 1, pp. 10–16, 1977, doi: https://doi.org/10.1002/aic.690230103.

[41] "PlusICE Range 2021-1 - PCM Products Ltd."

[42] Dion King and Robert Potter, "Description of Steady-State Cooling Plant Model Developed for Use in Evaluating Optimal Control of Ice Thermal Storage Systems," *ASHRAE Trans. 1998*, vol. 104, p. 12, Oct. 1998.

[43] K. H. Drees and J. E. Braun, "Modeling and Experimental Validation of Area Constrained Ice Storage Systems," presented at the International Refrigeration and Air Conditioning Conference, Purdue University: Purdue e-Pubs, 1994, p. 10.

[44] Gregor P. Henze and Moncef Krarti, "Predictive Optimal Control of Active and Passive Building Thermal Storage Inventory," University of Nebraska, DE-FC-26-01NT41255, Sept. 2001.

[45] H. Selvnes, Y. Allouche, R. I. Manescu, and A. Hafner, "Review on cold thermal energy storage applied to refrigeration systems using phase change materials," *Therm. Sci. Eng. Prog.*, vol. 22, p. 100807, May 2021, doi: 10.1016/j.tsep.2020.100807.

[46] H. Qiao, V. Aute, and R. Radermacher, "Transient modeling of a flash tank vapor injection heat pump system – Part I: Model development," *Int. J. Refrig.*, vol. 49, pp. 169–182, Jan. 2015, doi: 10.1016/j.ijrefrig.2014.06.019.

[47] A.-H. Othman, V. Aute, and J. Tancabel, "Recharge Demand Mitigation for Latent Heat Thermal Energy Storage at Off-peak Hours," in *8th International High-Performance Buildings Conference*, 2024.

[48] A.-H. Othman, V. Aute, and J. Tancabel, "Performance Assessment of a Dual-purpose HP-TES for a Typical Year Comparing Different Climate Zones," 2024.

[49] Xcel Energy, “Time of Use Rates.” Accessed: June 02, 2025. [Online]. Available: https://mn.my.xcelenergy.com/s/business/rate-plans/time-of-use

[50] FPL Northwest FL, “Time of Use Rates.” Accessed: June 02, 2025. [Online]. Available: https://www.fpl.com/northwest/rates/business-options.html

[51] K. H. Drees and J. E. Braun, “Development and Evaluation of a Rule-Based Control Strategy for Ice Storage Systems,” *HVACR Res.*, vol. 2, no. 4, pp. 312–334, Oct. 1996, doi: 10.1080/10789669.1996.10391352.

[52] A. A. Bani Issa, C. Liang, H. Liu, E. A. Groll, and D. Ziviani, “Experimental analysis of a liquid-to-liquid two-stage R290 heat pump system for residential cold-climate applications,” *Appl. Therm. Eng.*, vol. 278, p. 127223, Nov. 2025, doi: 10.1016/j.applthermaleng.2025.127223.

[53] “AHRI 550/590 (I-P) and 551/591 (SI): Performance Rating of Water-Chilling and Heat Pump Water-Heating Packages Using the Vapor Compression Cycle | AHRI.” Accessed: Dec. 09, 2025. [Online]. Available: https://www.ahrinet.org/search-standards/ahri-550590-i-p-and-551591-si-performance-rating-water-chilling-and-heat-pump-water-heating-packages

[54] *modelica/ModelicaStandardLibrary*. (Mar. 22, 2024). Modelica. Modelica Association. Accessed: Mar. 22, 2024. [Online]. Available: https://github.com/modelica/ModelicaStandardLibrary